INORGANIC CHEMISTRY
FRONTIERS

CHINESE CHEMICAL SOCIETY

ROYAL SOCIETY OF CHEMISTRY

RESEARCH ARTICLE

View Article Online
View Journal | View Issue

Cite this: *Inorg. Chem. Front.*, 2025, **12**, 1411

An *in situ* polymerization trial to prepare PEDOT decorated VO_2 hollow nanospheres for stable zinc ion storage at 0 °C

Chunru Zhao,[a] Yi Liu,[a] Yefei Xu,[b] Zhanyi Liu,[b] Mian Li,*[b] Qing Huang[b] and Xiang Wu*[a]

Received 5th December 2024,
Accepted 25th December 2024

DOI: 10.1039/d4qi03124e

rsc.li/frontiers-inorganic

Vanadium oxides possess a variety of crystal structures and have emerged as imperative cathode materials for zinc ion batteries in recent years. However, their further applications are largely restricted by their poor rate capability and cycling instability. In this work, we propose an *in situ* polymerization strategy to prepare novel VO_2 hollow nanospheres by PEDOT coating. The assembled Zn//VO_2@0.8PEDOT cells show a specific capacity of 455.8 mA h g^{-1} at a current density of 0.2 A g^{-1}. They can still maintain a retention rate of 85.5% after 3000 cycles at 5.0 A g^{-1}. Additionally, the soft-packaged devices demonstrate remarkable mechanical stability under diverse folding conditions.

Introduction

The emergence of large-scale energy storage systems and portable accessories has prompted researchers to concentrate on safe and cost-effective energy storage technologies.[1] In recent decades, lithium-ion batteries (LIBs) have become the preferred ones for the accumulator devices in electric vehicles owing to their high specific capacity and long cycle life.[2–4] However, their widespread application is hampered by the territorial distribution of lithium resources and high mining costs.[5] Therefore, it is imperative to seek many alternatives to LIBs, such as rechargeable aqueous metal ion batteries (Na, Mg, Ca and Zn).[6–9] Among them, zinc ion batteries (ZIBs) demonstrate a certain development prospect due to their high theoretical capacity (820 mA h g^{-1}) and abundant resources.[10] Various cathode materials have been reported for application in AZIBs, including manganese-based materials,[11,12] Prussian blue analogues[13–15] and vanadium-based products.[16,17]

Among them, vanadium oxides have attracted significant attention owing to their plentiful valence states and open frameworks.[18] The metastable phase VO_2(B) possesses a bilayer structure with large lattice spacing, based on edge-sharing VO_6 octahedra, which facilitates the rapid transfer of ions.[19] The introduction of conductive polymers results in excellent electrochemical performances in electrode materials due to the expansion of interlayer space and high electrical conductivity. In the literature, Liu's group designed an ice bath route to synthesize polypyrrole (PPy) coated VO_2(A) hollow spheres.[20] The fabricated VO_2-5@PPy electrodes deliver a specific capacity of 440 mA h g^{-1} at 0.1 A g^{-1}. Liu and co-workers[21] prepared PVO@PEDOT nanosheets through an *in situ* intercalation and polymerization process. The assembled batteries deliver an energy density of 363.4 W h kg^{-1} at a power density of 180 W kg^{-1}. Thus far, researchers have developed a variety of polymer modification strategies including polyaniline, polypyrrole and poly(3,4-ethylene dioxythiophene).[22–24]

Herein, we utilize a simple hydrothermal route to synthesize VO_2 hollow spheres. The fabricated devices present a specific capacity of 290.5 mA h g^{-1} at a current density of 0.2 A g^{-1} and maintain 107.2 mA h g^{-1} at 5.0 A g^{-1} after 1000 cycles. The VO_2 hollow spheres coated with PEDOT consist of many nanosheets with interconnections, which largely increase the conductivity of the electrodes. The as-obtained VO_2@0.8PEDOT samples deliver a specific capacity of 455.8 mA h g^{-1} at a rate of 0.2 A g^{-1}. Furthermore, they retain 275.9 mA h g^{-1} at 5.0 A g^{-1} even after 3000 cycles.

Experimental section

Preparation of VO_2 hollow spheres

The VO_2 samples were synthesized using a one-step hydrothermal process. Typically, 45 mL of deionized (DI) water was mixed with 0.7 g of NH_4VO_3 powder and stirred for 10 min at 80 °C. Next, 5 mL of 1 M HCl was added dropwise into the mixture for 5 min. Following that, 5 mL of $N_2H_4 \cdot H_2O$ was

---

[a] *School of Materials Science and Engineering, Shenyang University of Technology, Shenyang 110870, China. E-mail: wuxiang05@sut.edu.cn*
[b] *Zhejiang Key Laboratory of Data-Driven High-Safety Energy Materials and Applications, Ningbo Institute of Materials Technology and Engineering, Chinese Academy of Sciences, Ningbo 315201, China. E-mail: limian@nimte.ac.cn*

added to the mentioned solution and stirred for 1 h. The above solution was subsequently transferred to an 80 mL Teflon-lined stainless-steel autoclave and maintained at 120 °C for 4 h. The synthesized products were repeatedly washed with alcohol and DI water several times, dried overnight at 60 °C and then annealed at 350 °C for 3 h under an Ar atmosphere. The collected black powder was named VO_2.

Preparation of VO_2@PEDOT products

0.3 g of the VO_2 sample was dispersed in an autoclave with 50 mL of DI water for 5 min. Then, 0.5/0.8/1.1 mL of EDOT monomer was added to the above solution respectively and stirred continuously at 25 °C for 24 h. During the stirring, the color of the mixture changes from gray to blackish green. The dark green products were centrifuged multiple times and dried overnight at 60 °C. The as-prepared samples were labeled as VO_2@0.5PEDOT, VO_2@0.8PEDOT and VO_2@1.1PEDOT, respectively.

Synthesis of PAM gel electrolyte

20 mL of 3 M $Zn(CF_3SO_3)_2$ electrolyte were mixed with 2 g of acrylamide powder and stirred until completely dissolved. Next, 10 mg of potassium persulfate and 2 mg of *N*,*N*′-methylenebis(acrylamide) were added to the above solution and stirred for 1 h. Finally, the slurry was injected into a mold (100 mm × 70 mm × 2 mm) and heated at 60 °C for 2 h.

Electrochemical characterization

Coin-type cells were assembled with a cathode, anode (zinc foil), separator (glass fiber membrane) and electrolyte (3 M $Zn(CF_3SO_3)_2$). The active material (VO_2@0.8PEDOT), acetylene black (Super p) and polyvinylidene fluoride (PVDF) were combined in a gravimetric ratio of 7 : 2 : 1. Subsequently, the mixture was placed into *N*-methyl-1-2-pyrrolidone (NMP) solution to form a slurry, which was evenly distributed on carbon paper. The cathode possesses an average loading mass of approximately 1.5 mg g^{-1}. The galvanostatic charge–discharge (GCD) curves were recorded and the galvanostatic intermittent titration technique (GITT) was performed using a Neware CT-4008T automatic battery tester. Finally, an electrochemical workstation (CHI660E) was used for cyclic voltammetry (CV) and electrochemical impedance spectroscopy (EIS) studies. All the electrochemical experiments were conducted within a cut-off voltage window range from 0.2 to 1.4 V.

Material characterization

We utilized X-ray diffraction (XRD, Rigaku Ultima IV) to characterize the crystal structure. X-ray photoelectron spectroscopy (XPS, Thermo Scientific K-Alpha) was performed to ascertain the elemental composition of the samples. Then, their morphology and composition were observed by scanning electron microscopy (SEM, Gemini 300-71-31) and high-resolution transmission electron microscopy (HRTEM, FEI, Tecnai G2 F20). The surface and aperture structures were investigated using the Brunauer–Emmett–Teller (BJH, JW-TB220A) method. Finally, we measured the wettability of the electrode with a contact angle tester (JY-82C).

Results and discussion

First, we investigate the crystal structure and crystallinity of the samples by XRD, as shown in Fig. 1a. All diffraction peaks are indexed to the VO_2 phase (PDF#81-2392). Their lattice parameters are a = 12.093 Å, b = 3.702 Å and c = 6.433 Å. The typical peaks at 15.30°, 25.23°, 30.29°, 33.75°, 44.94°, 49.18°, 59.18° and 68.81° correspond to the (200), (110), (111), (−311), (−601), (020), (−404) and (−621) crystal planes. Furthermore, the VO_2@0.8PEDOT product presents strong peaks in the (200), (110) and (−311) planes, showing its excellent crystallinity.

Then, XPS is used to determine the elemental valence distribution of the samples. The V, O, C and N elements are shown in the full spectra (Fig. 1b). The V 2p spectra include $2p_{1/2}$ and $2p_{3/2}$ orbitals (Fig. 1c). The two peaks observed at 516.5 and 523.6 eV are deconvoluted into V^{4+}, while the peaks at 517.7 and 525.1 eV are assigned to V^{5+}.[25] Fig. 1d presents the O 1s spectra at 532.52 and 531.26 eV, corresponding to V–O and O_d, respectively.[26] As seen in Fig. 1e, the C 1s spectra are split into three peaks, including the C–C bond at 284.8 eV, the C–O bond at 285.7 eV and C═O at 288.8 eV.[27] As seen in Fig. 1f, the VO_2@0.8PEDOT product demonstrates a larger specific surface area (82.654 m^2 g^{-1}) than the VO_2 material (53.337 m^2 g^{-1}). It suggests that the large specific surface area provides abundant active sites for the storage capacity of zinc ions.[28]

We further observe the morphologies and structures of the samples by SEM and TEM. Fig. 2a and b show that VO_2 products present a hollow sphere shape. After the *in situ* polymerization of PEDOT, the nanoribbons are cross-linked with each other to form a porous network structure (Fig. 2c and d). It facilitates the penetration of electrolyte and the transfer of zinc ions.[29] The HRTEM images (Fig. 2e) clearly demonstrate a layer with amorphous characteristics on the surface of the samples. The lattice spacing of 0.206 nm corresponds to the (−601) crystal plane of the VO_2 phase. The elemental mappings indicate that four elements (V, O, C and S) are uniformly distributed along the surface of the materials, as shown in Fig. 2f.

Subsequently, the obtained samples as cathodes are assembled into a series of coin-type cells to investigate the electrochemical kinetic behavior of the electrodes. The initial three CV curves of the VO_2@0.8PEDOT electrodes are illustrated in Fig. 3a, which recorded the voltage window of 0.2–1.4 at a scan rate of 0.1 mV s^{-1}. Fig. 3b shows the cycling performance at 0.2 A g^{-1}. The fabricated Zn//VO_2@0.8PEDOT cells deliver an initial specific capacity of 455.8 mA h g^{-1}. The specific capacity of the composites is significantly improved compared to that of Zn//VO_2 batteries (278.3 mA h g^{-1}). The platform of the GCD curves (Fig. 3c) is consistent with the redox peaks (1.03/0.92 and 0.72/0.47) of the CV curves.

Also, the rate capability of the batteries is a significant parameter in assessing their commercial applications. As depicted in Fig. 3d, the VO_2@0.8PEDOT coin-type cells show specific capacities of 479.6, 463.4, 443.7, 427.5, 404.6 and 349.4 mA h g^{-1} at 0.1, 0.2, 0.5, 1.0, 2.0 and 5.0 A g^{-1}. A specific capacity of

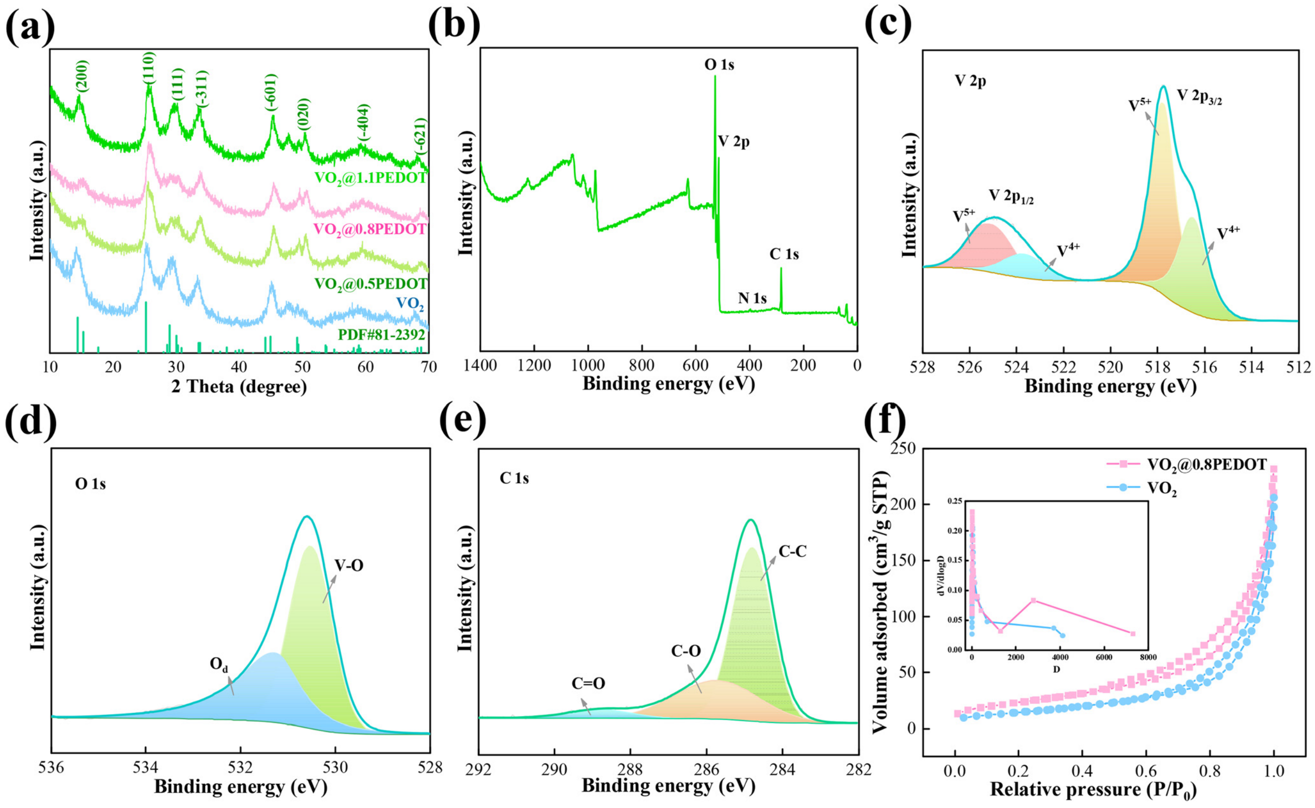

Fig. 1 The crystal structure and chemical composition. (a) XRD patterns, (b) XPS full spectra, (c) V 2p, (d) O 1s, (e) C 1s, and (f) N_2 adsorption–desorption isotherms; the inset shows the pore size distributions of the VO_2 and VO_2@0.8PEDOT products.

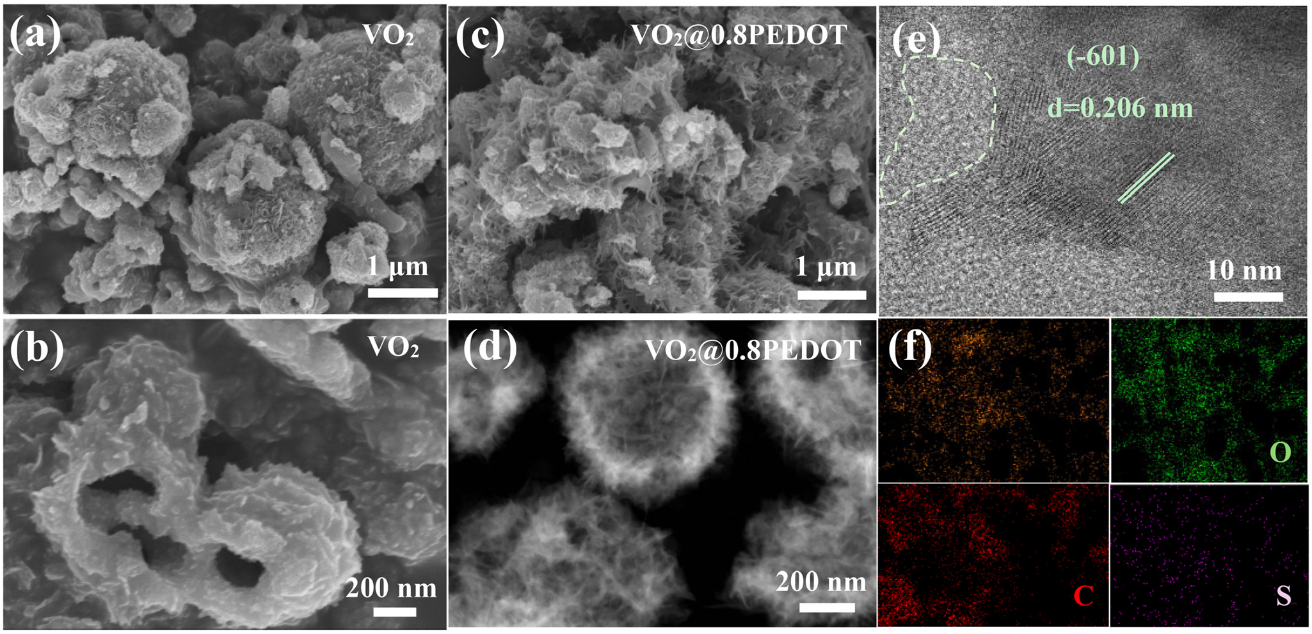

Fig. 2 SEM images: (a and b) VO_2 and (c) VO_2@0.8PEDOT samples, (d) TEM image, (e) HRTEM images, and (f) EDS elemental mapping.

470.3 mA h g^{-1} (98.0% of the initial discharge capacity) is retained when the current density recovers to 0.1 A g^{-1}. From Fig. 3e, the VO_2@0.8PEDOT materials are further studied at a current density of 5.0 A g^{-1} to evaluate the cycling stability of the batteries. The VO_2@0.8PEDOT cells deliver a specific capacity of 425.8 mA h g^{-1} at 5.0 A g^{-1} after 80 cycles acti-

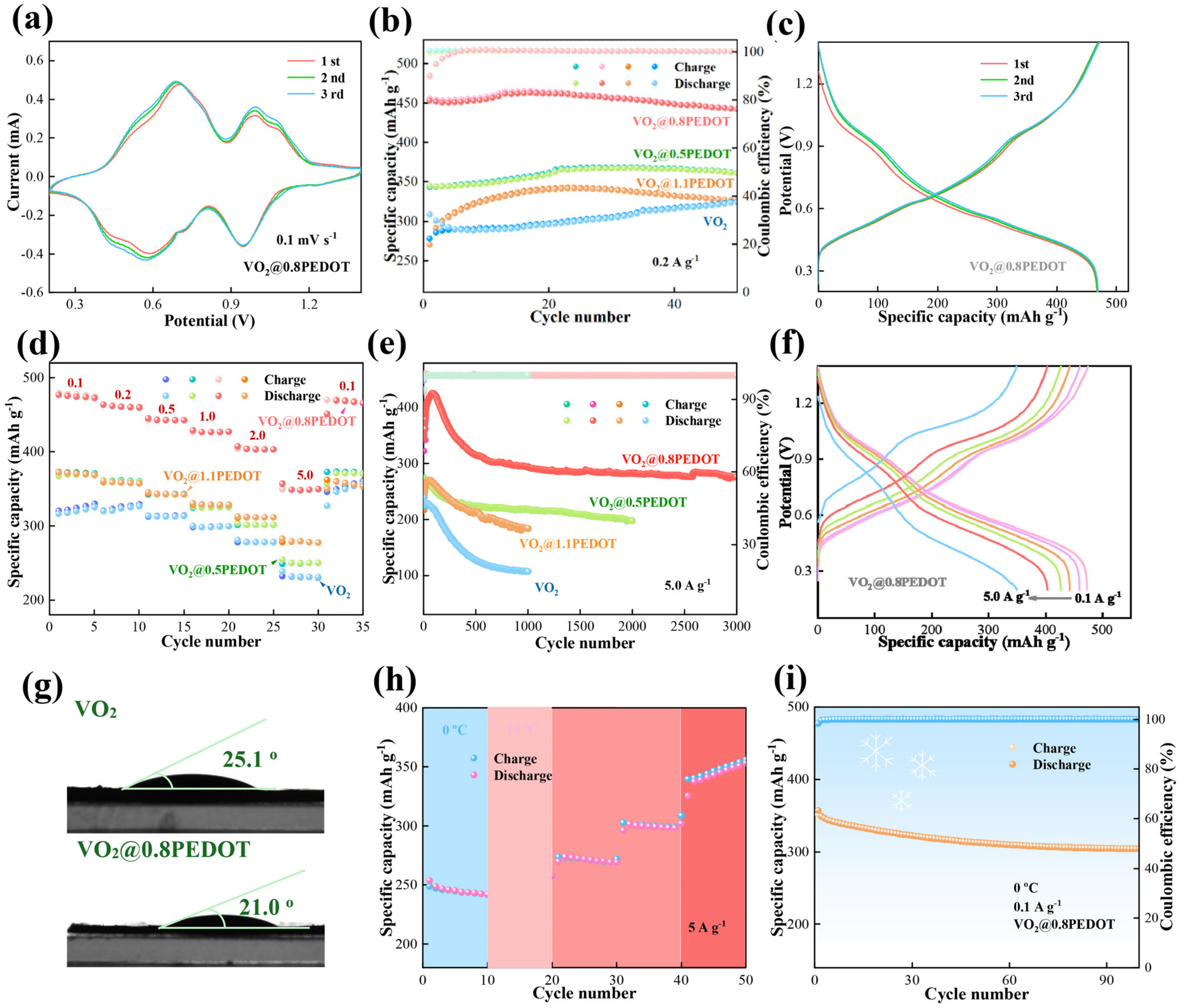

Fig. 3 Electrochemical performance. (a) CV curves of VO_2@0.8PEDOT at 0.1 mV s^{-1}, (b) cyclability at 0.2 A g^{-1}, (c) GCD curves of VO_2@0.8PEDOT electrodes at 0.1 A g^{-1}, (d) long-term cycles at 5.0 A g^{-1}, (e and f) rate performance, (g) contact angle of the electrolyte (3 M $Zn(CF_3SO_3)_2$) on the VO_2 and VO_2@0.8PEDOT cathodes, (h) different temperatures, and (i) cycling performance at 0 °C.

vation. Moreover, they maintain a retention rate of 80.0% after 3000 cycles. The excellent mechanical stability is ascribed to the large contact area between the electrode and the electrolyte.[30] Nevertheless, VO_2 materials possess a retention rate of 47.5% after 1000 cycles. This is attributed to the repetitive embedded and detachment process of zinc ions, which ultimately leads to structural collapse.[31] Fig. 3f presents the corresponding charge/discharge curves from 0.1 to 5.0 A g^{-1}. It reveals that when the current density increases, the capacity decreases.

The interface behaviors of the VO_2 and VO_2@0.8PEDOT cathodes are first characterized through a water contact angle test. The contact angle (Fig. 3g) of the electrolyte (3 M $Zn(CF_3SO_3)_2$) on the VO_2 cathode reaches 25.1°, which is larger than that (21.0°) of the VO_2@0.8PEDOT cathode. Fig. 3h presents the variation of specific capacities with the change in the working temperature of the as-assembled batteries. The specific capacity of the device increases linearly with the temperature. When the temperature is 60 °C, the cell provides a specific capacity of 355.8 mA h g^{-1} at a current density of 5.0 A g^{-1}. The specific capacitance retention of Zn//VO_2@0.8PEDOT is 87.5% at 0 °C after 100 cycles, as shown in Fig. 3i.

Also, we explore the electrochemical reaction kinetics of the battery and the storage behavior of zinc ions. Fig. 4a demonstrates the CV curves of the batteries at various scan rates from 0.1 to 0.5 mV s^{-1}. With the increase in the scan rate, the CV curve presents a similar shape. The oxidation peaks shift to a high voltage region, while the reduction peaks move to a low one. From Fig. 4b, according to the formula $i = av^b$, the calculated fitted b values are 1.14, 0.90, 0.92 and 0.91, which are all

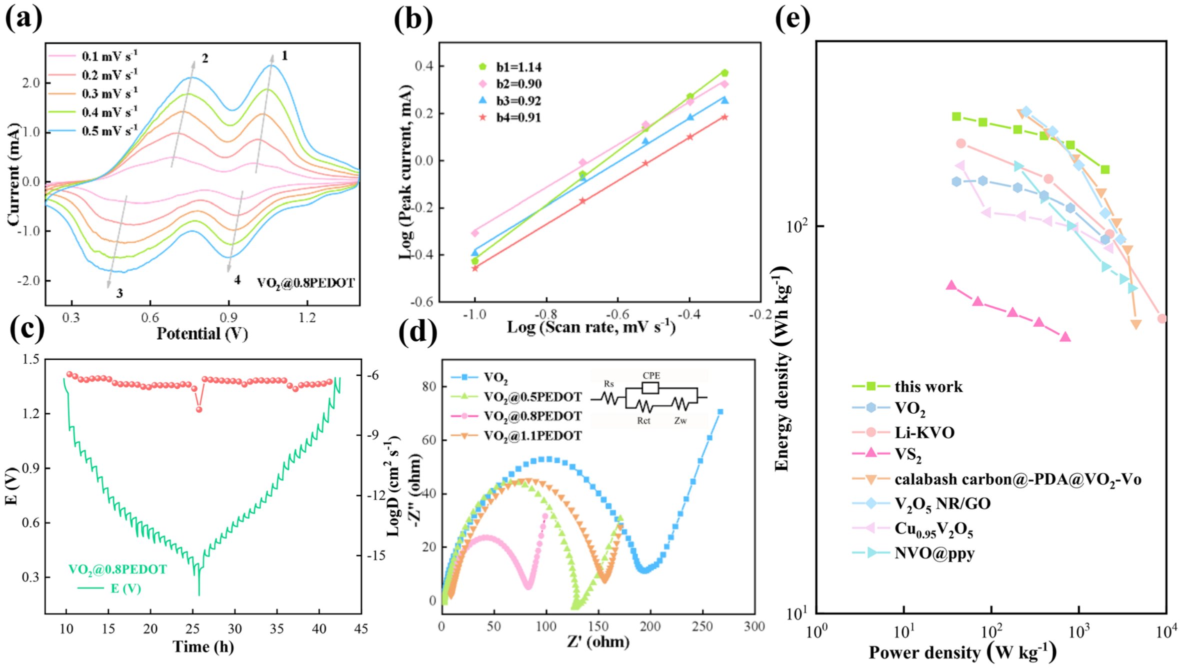

Fig. 4 Electrochemical mechanism. (a) CV curves and (b) log(i) *versus* log(v) of the VO_2@0.8PEDOT electrode, (c) GITT curves, (d) Nyquist plots, and (e) Ragone plot of VO_2@0.8PEDOT.

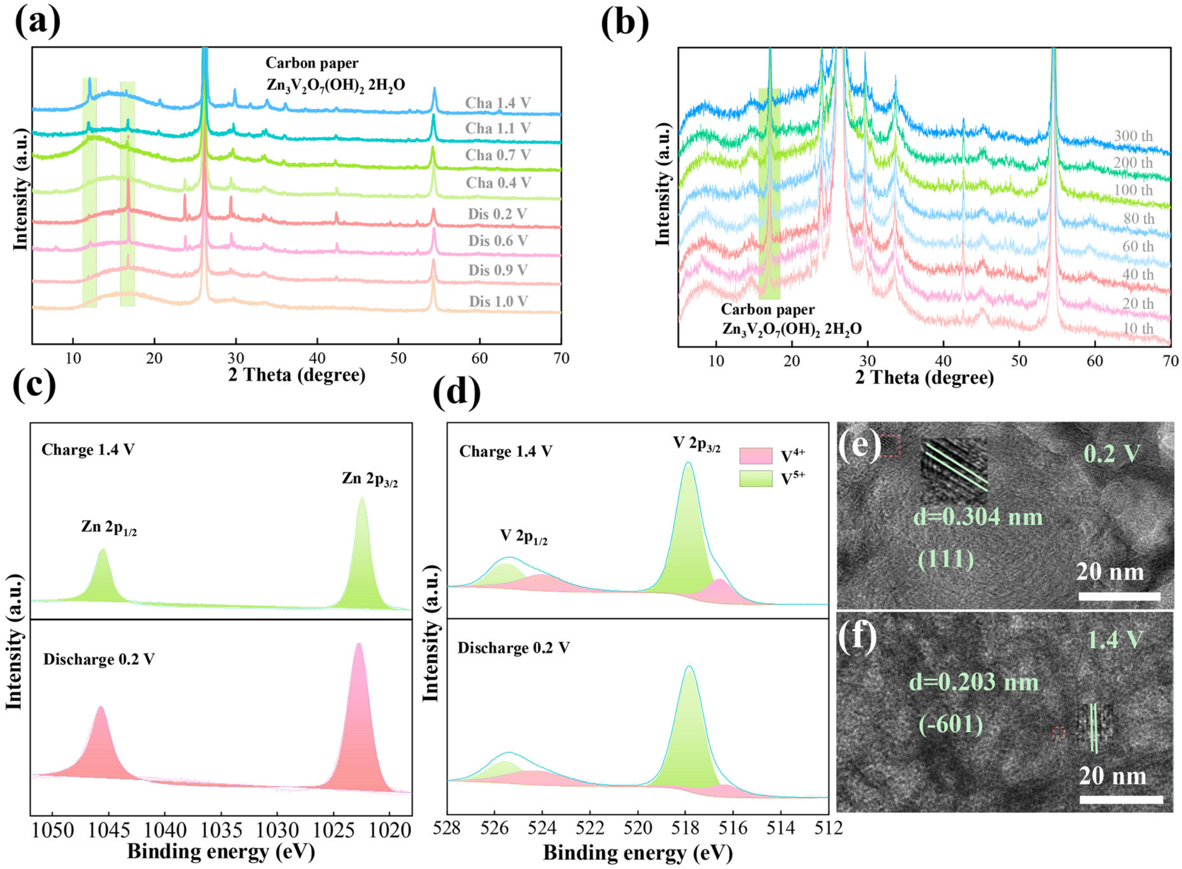

Fig. 5 Structural characterization. (a and b) *Ex situ* XRD patterns, (c and d) XPS spectra, and (e and f) HRTEM images.

close to 1.[32] The results indicate that the capacitive behavior is dominant during charging.[33] Then, the GITT curves are used to assess the diffusion capability of Zn^{2+} and the D_{Zn} value of the VO_2@0.8PEDOT electrode materials varies between 10^{-6} and 10^{-8} cm^2 s^{-1} (Fig. 4c). This result shows that VO_2@0.8PEDOT enables the rapid transfer of charge to the electrode. EIS measurement is performed to further study the electrochemical behavior of the batteries. Also, the Nyquist plots are depicted in Fig. 4d, and the inset shows the schematic of the corresponding equivalent circuit. The VO_2@0.8PEDOT samples possess a lower charge transfer resistance (R_{ct}) than VO_2 products. This suggests that there is a fast ion diffusion process within the electrodes. Fig. 4e demonstrates the Ragone plot of VO_2@0.8PEDOT and other vanadium-based electrode materials. The Zn//VO_2@0.8PEDOT batteries show an energy density of 177.4 W h kg^{-1} at a power density of 200 W kg^{-1}, which is better than that in previous reports.[34–39]

To investigate the electrochemical reaction mechanism, *ex situ* XRD and XPS are utilized to study the storage mechanism and structural evolution of VO_2@0.8PEDOT samples. Fig. 5a presents the XRD patterns of the electrode in different charging and discharging stages. When the charge voltage decreases from 1.4 V to 0.2 V, the (−311) crystal plane moves

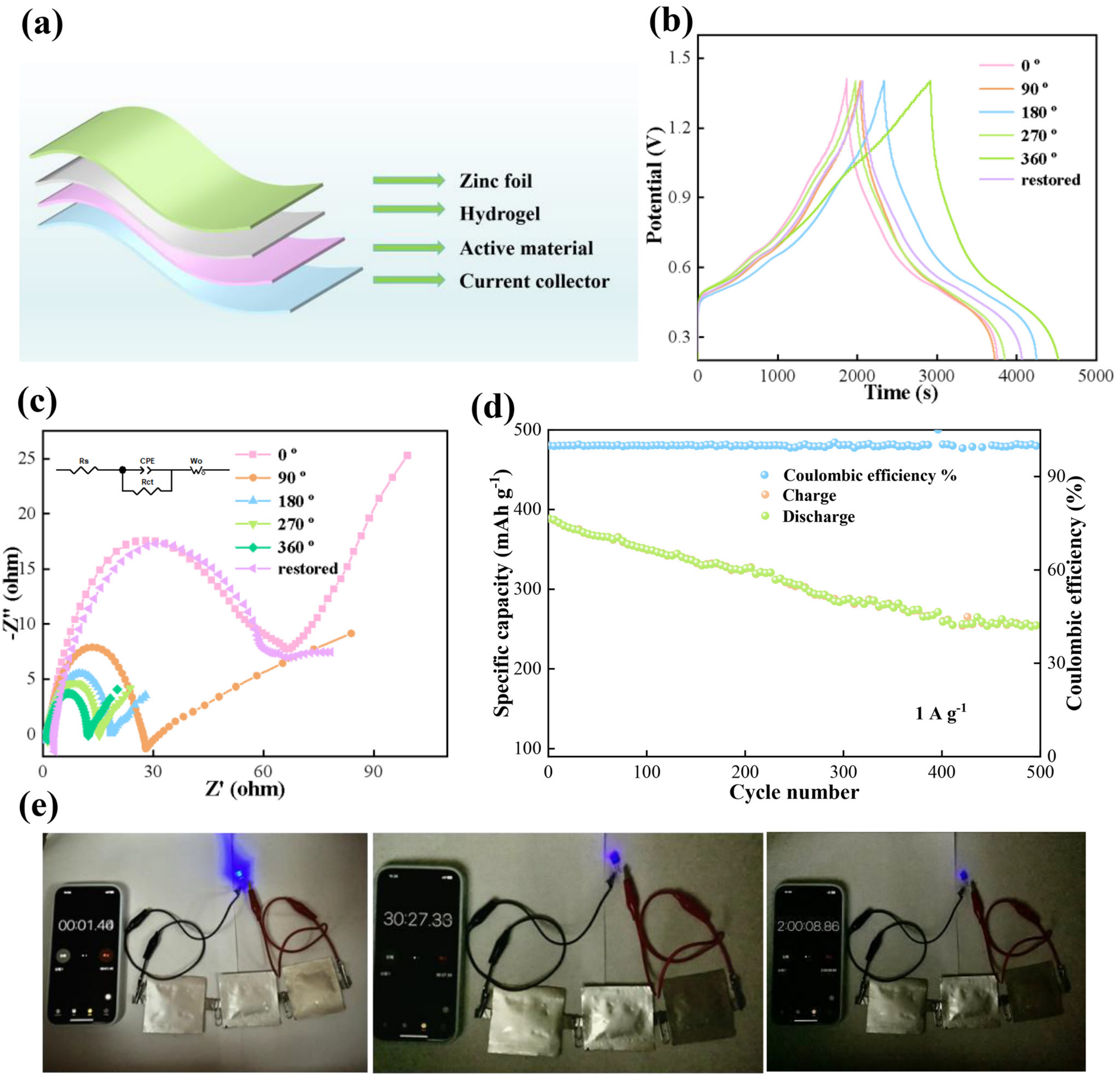

Fig. 6 (a) Structure schematic of the flexible device, (b) GCD curves in the 1.0 A g^{-1} state, (c) EIS, (d) long-term cycles at 1.0 A g^{-1}, and (e) digital photos of the blue LED.

from the low-angle region to the high-angle region. This is due to the expansion of the interlayer spacing of VO_2@0.8PEDOT materials with the insertion of water molecules and zinc ions during the reaction.[40] The diffraction peaks at 12.2° and 16.9° correspond to the (001) and (100) crystal planes of $Zn_3V_2O_7(OH)_2\cdot 2H_2O$ (ZVO, JCPDS no. 87-0417) phases. This indicates that zinc ions are intercalated into the host successfully. The electrochemical reaction process can be expressed as follows:[41]

$$V^{5+} + 4H_2O \rightarrow VO_2(OH)_2^{\ -} + 6H^+ \tag{1}$$

$$2VO_2(OH)_2^{\ -} + 3Zn^{2+} + 3H_2O \rightarrow Zn_3V_2O_7(OH)_2 \cdot 2H_2O + 4H^+ \tag{2}$$

Fig. 5b shows the *ex situ* XRD patterns at a working temperature of 0 °C with different cycling times. Moreover, the byproducts are obtained by the reaction of OH^- and $Zn(CF_3SO_3)_2$ and the reaction of Zn^{2+} and V^{5+}, respectively. According to previous reports, OH^- is produced from the breaking of water molecules, which provides indirect evidence that protons are involved in the charge–discharge process.[42]

Subsequently, we use *ex situ* XPS to explore the valence change and chemical constitution of VO_2@0.8PEDOT samples. The peak intensity of Zn 2p spectra in the completely charged and discharged states indicates that Zn^{2+} is successfully embedded/de-embedded in electrode lattices (Fig. 5c).[43] Fig. 5d shows the *ex situ* V 2p spectra of the VO_2@0.8PEDOT electrode in various states. The peak area of different valence states changes with the change of charge and discharge states.[44] The result indicates the high reversibility of the PEDOT coated VO_2 electrode during the insertion/extraction of Zn^{2+}.[45] Moreover, HRTEM is utilized to explore the reversibility of the structural evolution process, as seen in Fig. 5e and f. When the VO_2@0.8PEDOT electrode is discharged to 0.2 V, the (111) plane is extended to lattice fringes with a spacing of 0.304 nm due to the embedding of Zn^{2+}. In the fully charged state, the (−601) plane recovers a spacing of 0.203 nm. This suggests that the VO_2@0.8PEDOT electrode possesses high structural stability.

Finally, a multitude of soft-packaged devices are fabricated to investigate the practical application of VO_2@0.8PEDOT products. Fig. 6a shows the structural schematic of a flexible battery. Fig. 6b shows the GCD curves of the flexible device at various folding angles at 1.0 A g^{-1}. The discharging time is extended with an increase in the bending angle owing to full contact between the electrode and hydrogel electrolyte. Fig. 6c shows that the R_{ct} values gradually decrease as the folding degree changes. The excellent mechanical stability is further demonstrated by the fact that it still restores to the initial state in the subsequent folding process. The soft-packaged device provides a retention ratio of 64.6% after 500 cycles at 1.0 A g^{-1} (Fig. 6d). Finally, a blue LED is lit by connecting three VO_2@0.8PEDOT devices in series for 2 h, as shown in Fig. 6e.

Conclusion

In general, we have prepared zinc ion batteries with PEDOT coated VO_2 products as the cathode and 3 M $Zn(CF_3SO_3)_2$ as the electrolyte. The specific surface area and active sites are significantly increased by the addition of the PEDOT surfactant. Moreover, the Zn//VO_2@0.8PEDOT batteries demonstrate fast reaction kinetics and long-term cycle life. The electrical conductivity of PEDOT enhances the efficiency of electron and ion transport. Also, the as-fabricated cells show excellent specific capacity and rate performance at high current density. The full cells present outstanding mechanical durability at 0 °C. The soft-packaged cells achieve stable cycling, showing their promising potential for future energy storage applications.

Author contributions

Chunru Zhao, Yi Liu, Yefei Xu and Zhanyi Liu: conceptualization, software, data curation and writing – original draft. Xiang Wu, Mian Li and Qing Huang: supervision and writing – review and editing.

Data availability

The data supporting this article have been included in the submitted article.

Conflicts of interest

The authors declare no conflicts of interest.

Acknowledgements

The work is supported by the National Natural Science Foundation of China (no. 52472227).

References

1 Y. Liu, P. Hu, H. Liu, J. Song, A. Umar and X. Wu, Toward a high performance asymmetric hybrid capacitor by electrode optimization, *Inorg. Chem. Front.*, 2019, **6**, 2824–2831.

2 R. Cang, K. Ye, K. Zhu and D. Cao, Environmentally friendly and flexible aqueous zinc ion batteries using an organic anode and activated carbon as the cathode, *ACS Sustainable Chem. Eng.*, 2023, **11**, 5065–5071.

3 C. Yu, S. Huang, H. Xu, J. Yan, K. Rong and M. Sun, Optimal charging of lithium-ion batteries based on lithium precipitation suppression, *J. Energy Storage*, 2024, **82**, 110580.

4 T. Zeng, D. H. Liu, C. Fan, R. Fan, F. Zhang, J. Liu and Z. Chen, $LiMn_{0.8}Fe_{0.2}PO_4$@C cathode prepared via a novel

hydrated $MnHPO_4$ intermediate for high performance lithium-ion batteries, *Inorg. Chem. Front.*, 2023, **10**, 1164–1175.

5 Q. Yan, Z. Hu, Z. Liu, F. Wu, Y. Zhao, R. Chen and L. Li, Synergistic interaction between amphiphilic ion additive groups for stable long-life zinc ion batteries, *Energy Storage Mater.*, 2024, **67**, 103299.

6 M. Zhao, S. Li, X. Wu and L. Sun, Regulating oxygen vacancies in ammonium vanadate electrode materials for advanced aqueous zinc ion batteries, *iScience*, 2024, **27**, 110926.

7 Q. Sun, S. Luo, R. Huang, Q. Liu, S. Yan and X. Lin, Insights on solid electrolytes for solid-state magnesium batteries: Progress and prospects, *Energy Storage Mater.*, 2024, **70**, 103508.

8 Y. Liu, Y. Liu and X. Wu, Rational design of bi-phase CaV_2O_6/NaV_6O_{15} cathode materials for long-life aqueous zinc batteries, *EcoMat*, 2023, **5**, e12409.

9 X. Li, Z. Chen, Y. Yang, S. Liang, B. Lu and J. Zhou, The phosphate cathodes for aqueous zinc-ion batteries, *Inorg. Chem. Front.*, 2022, **9**, 3986–3998.

10 D. Zhang, J. Cao, X. Zhang, J. Qin and Z. Zeng, Architecting a high-energy-density rocking-chair zinc-ion batteries via carbon-wrapped vanadium dioxide, *ACS Appl. Mater. Interfaces*, 2023, **15**, 57230–57238.

11 C. Yin, C. Pan, Y. Pan and J. Hu, Hollow Mn-Co-O@C yolk-shell microspheres with carbon shells as cathodes derived from a double-metal MOF for aqueous zinc-ion batteries, *ACS Sustainable Chem. Eng.*, 2023, **11**, 12397–12405.

12 Y. Liao, C. Yang, J. Bai, Q. He, H. Wang, H. Chen and L. Chen, Insights on cycling stability of manganese-based zinc-ion batteries: From energy storage mechanisms to capacity fluctuation and optimization strategies, *Chem. Sci.*, 2024, **15**, 7441–7473.

13 Y. Xiao, J. Xiao, H. Zhao, J. Li, G. Zhang, D. Zhang and H. Liu, Prussian blue analogues for sodium–ion battery cathodes: A review of mechanistic insights, current challenges, and future pathways, *Small*, 2024, **20**, 2401957.

14 X. Fu, L. Zhang, C. Wang, H. Sun and X. Yang, Recent progress of prussian blue analogues as cathode materials for metal ion secondary batteries, *Rare Met.*, 2024, 1–26.

15 J. Liu, Z. Shen and C. Lu, Research progress of prussian blue and its analogues for cathode of aqueous zinc ion battery, *J. Mater. Chem. A*, 2024, **12**, 2647–2672.

16 T. Zhou and G. Gao, Pre-intercalation strategy in vanadium oxides cathodes for aqueous zinc ion batteries: Review and prospects, *J. Energy Storage*, 2024, **84**, 110808.

17 X. Dou, X. Xie, S. Liang and G. Fang, Low-current-density stability of vanadium-based cathodes for aqueous zinc-ion batteries, *Sci. Bull.*, 2024, **69**, 833–845.

18 Y. Liu, Y. Liu and X. Wu, Defect engineering of vanadium-based electrode materials for zinc ion battery, *Chin. Chem. Lett.*, 2023, **34**, 107839.

19 L. Kou, Y. Wang, J. Song, T. Ai, W. Li, P. Wattanapaphawong and K. Kajiyoshi, One-dimensional tunnel $VO_2(B)$ cathode materials for high-performance aqueous zinc ion batteries: A mini review of recent advances and future perspectives, *Green Chem.*, 2024, **26**, 1709–1724.

20 Y. Liu, P. Hu, H. Liu, X. Wu and C. Zhi, Tetragonal VO_2 hollow nanospheres as robust cathode material for aqueous zinc ion batteries, *Mater. Today Energy*, 2020, **17**, 100431.

21 Y. Liu, T. Wang, Y. Sun, M. Zhang, G. Gao, J. Yang and K. Cai, Fast and efficient *in situ* construction of low crystalline PEDOT-intercalated V_2O_5 nanosheets for high-performance zinc-ion battery, *Chem. Eng. J.*, 2024, **484**, 149501.

22 Y. Zhang, Z. Cao, S. Liu, Z. Du, Y. Cui, J. Gu and S. Yang, Charge–enriched strategy based on MXene–based polypyrrole layers toward dendrite–free zinc metal anodes, *Adv. Energy Mater.*, 2022, **12**, 2103979.

23 Y. Zhang, Y. Du, B. Song, Z. Wang, X. Wang, F. Wan and X. Ma, Manganese-ions and polyaniline Co-intercalation into vanadium oxide for stable zinc-ion batteries, *J. Power Sources*, 2022, **545**, 231920.

24 T. Schoetz, B. Craig, P. de Leon, A. Bund, M. Ueda and C. Low, Aluminium-Poly (3,4-Ethylenedioxythiophene) rechargeable battery with ionic liquid electrolyte, *J. Energy Storage*, 2020, **28**, 101176.

25 W. Shi, B. Yin, Y. Yang, M. Sullivan, J. Wang, Y. Zhang and J. Xue, Unravelling V_6O_{13} diffusion pathways via CO_2 modification for high-performance zinc ion battery cathode, *ACS Nano*, 2021, **15**, 1273–1281.

26 Z. Zhang, B. Xi, X. Wang, X. Ma, W. Chen, J. Feng and S. Xiong, Oxygen defects engineering of $VO_2{\cdot}xH_2O$ nanosheets via in situ polypyrrole polymerization for efficient aqueous zinc ion storage, *Adv. Funct. Mater.*, 2021, **31**, 2103070.

27 Y. Li, X. Liao, B. Xie, Y. Li, Q. Zheng and D. Lin, Hollow VO_2 microspheres anchored on graphene as advanced cathodes for aqueous zinc-ion batteries, *J. Colloid Interface Sci.*, 2024, **662**, 404–412.

28 S. Li, M. Zhao, D. Zhang and X. Wu, High-capacity aqueous Zn/MnO_2 batteries: A clue of K ion preintercalation, *Cryst. Growth Des.*, 2023, **23**, 8156–8162.

29 Y. Liu and X. Wu, Metal-organic framework assisted design of ZnVOx cathode for aqueous zinc batteries at extreme work condition, *Nano Energy*, 2024, **127**, 109809.

30 Y. Liu and X. Wu, High durable aqueous zinc ion batteries by synergistic effect of V_6O_{13}/VO_2 electrode materials, *J. Energy Chem.*, 2023, **87**, 334–341.

31 F. Wu, Y. Jiang, Z. Ye, Y. Huang, Z. Wang, S. Li and R. Chen, A 3D flower-like VO2/MXene hybrid architecture with superior anode performance for sodium ion batteries, *J. Mater. Chem. A*, 2019, **7**, 1315–1322.

32 M. Zhao, S. Li, A. Umar and X. Wu, $(NH_4)_2V_{10}O_{25}{\cdot}8H_2O$ nanowire materials for stable zinc ion storage, *Mater. Today Chem.*, 2023, **33**, 101686.

33 N. Wang, H. Liu, M. Sun, X. Ren, L. Hu, Z. Li and C. Jia, Achieving wide-temperature-range sustainable zinc-ion batteries via magnesium-doped cathodes and gel electrolytes, *ACS Sustainable Chem. Eng.*, 2024, **12**, 3527–3537.

34 P. Qi, H. Wang, L. Li, X. Shen, L. Ou, M. Chen and Y. Tang, Facile synthesis of oxygen-vacancy-rich Li-K coinsertion vanadate nanoflakes for high-performance zn-ion batteries, *ACS Sustainable Chem. Eng.*, 2023, **11**, 14691–14700.

35 S. Zhao, Y. Liu and X. Wu, Rose-shaped VS_2 nanosheets as cathode materials for rechargeable zinc ion batteries, *CrystEngComm*, 2023, **25**, 1986–1992.

36 X. Liu, Z. Xu, J. Wu, K. Wang and C. Yu, Synergistic effect of oxygen defects and calabash-like hollow carbon matrix enables VO_2 as high-performance cathode for zinc ion battery, *J. Colloid Interface Sci.*, 2025, **678**, 35–44.

37 K. Muthukumar, S. Rajendran, A. Sekar, Y. Chen and J. Li, Synthesis of V_2O_5 nanoribbon-reduced graphene oxide hybrids as stable aqueous zinc-ion battery cathodes via divalent transition metal cation-mediated coprecipitation, *ACS Sustainable Chem. Eng.*, 2023, **11**, 2670–2679.

38 X. Yu, F. Hu, Z. Guo, L. Liu, G. Song and K. Zhu, High-performance $Cu_{0.95}V_2O_5$ nanoflowers as cathode materials for aqueous zinc-ion batteries, *Rare Met.*, 2022, **41**, 29–36.

39 H. Du, M. Zhang, H. Zhang and X. Lei, Long cycle life and high rate aqueous zinc-ion batteries enabled by polypyrrole bridging ammonium vanadium bronze nanosheet cathodes, *J. Alloys Compd.*, 2023, **939**, 168669.

40 J. Cao, D. Zhang, Y. Yue, X. Yang, C. Yang, J. Niu and J. Lu, Unveiling the X–Ray absorption chemistry of $H_{3.78}V_6O_{13}$ cathode for aqueous zinc–ion batteries, *Adv. Funct. Mater.*, 2023, **33**, 2307270.

41 C. Zhao, Y. Liu, X. Wu and S. Luo, Graphene oxide wrapped VO_2 nanobelts for calendar–life Zn storage devices, *Adv. Sustainable Syst.*, 2024, **8**, 2400077.

42 Y. Liu, Y. Liu, X. Wu and Y. Cho, General carbon modification avenue to construct highly stable V_2O_5 electrodes for aqueous zinc-ion batteries, *ACS Sustainable Chem. Eng.*, 2023, **11**, 13298–13305.

43 D. Sun, Z. Wang, T. Tian, X. Yu, D. Yu, X. Zhou and Z. Lei, Constructing oxygen deficiency-rich V_2O_3@PEDOT cathode for high-performance aqueous zinc-ion batteries, *Rare Met.*, 2024, **43**, 635–646.

44 P. Luo, W. Zhong, W. Zhang, M. Zhou, W. Tang, H. Tang and Q. An, Trigger a multi-electron reaction by tailoring electronic structure of VO_2 toward more efficient aqueous zinc metal batteries, *J. Colloid Interface Sci.*, 2024, **666**, 371–379.

45 C. Zhao, Y. Liu, S. Li, X. Wu and J. Liu, PVP decorated $H_{3.78}V_6O_{13}$ microspheres assembled by nanosheets for aqueous zinc ion batteries at variable work temperature, *Chin. Chem. Lett.*, 2025, **36**, 110185.